ISSN 2766-2624

Methane Production from Carbondioxide in Polluted Areas Using Graphene Doped Ni/ NiO Nanocomposite via Photocatalysis

Advances in Earth and Environmental Science

Research Article

Delia Teresa Sponza*, Rukiye Öztekin

Dokuz Eylül University, Engineering Faculty, Environmental Engineering Department, Buca -İzmir Turkey

***Correspondence authors**

Delia Teresa Sponza
Dokuz Eylül University
Engineering Faculty
Environmental Engineering Department
Buca -İzmir Turkey

Submitted : 23 Sept 2021 ; Published : 8 Oct 2021

Abstract

Background: *Photocatalysis for the production of solar fuels and particularly to perform CO_2 reduction with a sufficiently high efficiency depends to the presence of H_2 and absence of H_2O using graphene doped Ni/ NiO nanocomposite.*

Objective: *To examine the methane production from carbondioxide in polluted areas using graphene doped Ni/ NiO nanocomposite via photocatalysis with the use of dimethylaniline and xylene as electron donors.*

Methods: *With 2 mg/l graphene doped Ni/ NiO nanocomposite with a Ni content of 19% wt from 786 µmol/h CO_2 gas 563 µl CH_4/g Ni.h was obtained at 160oC temperature and the quantum yield was detected as 1.99%. It was found that H_2O has a negative influence on the photocatalytic activity. Under continuous flow operation, water molecules were easier desorbed from the graphene doped Ni/NiO photocatalyst*

Results: *The maximum CH_4 production rate was 650 µl/h for 2.4 mg of graphene doped Ni/ NiO nanocomposite after a detectione time of 17 min. Dimethylaniline and xylene were used as electron donors and 1.2 ml/l dimethylaniline and 0.9 ml/l xylene enhanced the CH_4 productions by 8% and 12% as quenching factor.*

Conclusion: *Photocatalysis methods was effected for methane production from carbondioxide in polluted areas using graphene doped Ni/ NiO nanocomposite with the use of dimethylaniline and xylene as electron donors.*

Keywords: Carbondioxide; graphene doped Ni/NiO; methane; nanocomposite; nanoparticle; photocatalysis.

Introduction

The continuous increase in atmospheric CO_2 concentration is considered to be a key driver that induces climate change [1]. The prospect of unwanted climate change or climate heating–desertification has compelled investigations into the means to normalize atmospheric CO_2 concentrations. As is well known, CO_2 is a highly stable molecule, requiring significant energy input for its reduction [2]. In this regard, sunlight is considered to be the most useful energy source for promoting CO_2 conversion into useful hydrocarbon products, such as methane or ethane, offering the possibility of turning sunlight into fuels compatible with the current energy infrastructure [3].

Diminishing fossil fuel resources and increasing the atmospheric level of CO_2 have raised great concerns in recent years regarding future energy supply, and controlling the effects on global climate [4-6]. Natural photosynthesis is a process in which CO_2 is reduced in the presence of water, and carbohydrates and oxygen are produced, which is a solar to chemical energy conversion. This natural process has attracted a great deal of attention by researchers as a promising strategy to supply alternative energy and response the demand for global energy [5,6]. More than 100 years ago, Giacomo Ciamician suggested to implement the science of photosynthesis for designing solar fuels [7]. Given that, the photocatalytic reduction of CO_2 into hydrocarbons, which is so-called artificial photosynthesis, has been considered as an efficient approach [5]. Being thermodynamically stable (bond enthalpy of C = O in CO_2 is +805 kJ/mol), and unable to absorb light in the wavelengths of 200–900 nm, photoreduction of CO_2 is a difficult task, and needs an appropriate photosensitizer, such as a semiconductor catalyst. Despite the difficulties accompanied by this process, the potential rewards are well worth a try [8]. Therefore, much more efforts have been put in practice to attain the following goals:

1. reducing the complications of global warming, resulted from the increased atmospheric CO_2 concentration;
2. utilization of clean hydrocarbon fuels, such as methane, methanol, and ethane, as fossil fuel alternatives; and

3. developing facile and clean methods using sunlight as unlimited source of energy [9].

The photoreduction of CO_2 consists of multi-electron steps, which leads to various products such as CO, CH4, higher hydrocarbons, alcohols, aldehydes, and carboxylic acids [10]. The mechanism of this process is rather complex, so that trying the potential pathways, simultaneously terminates to different products. This has inspired many researchers to focus on investigating the mechanism and controlling the selectivity of the reaction. The following criteria are generally required for an effective system used for photoreduction of CO_2:

1. more positive redox potential for the photo-induced holes on the valence band (VB) of the semiconductor compared to the redox potential of O_2/H_2O;
2. more negative redox potential for the photo-generated electrons on the conduction band (CB) of the semiconductor in relation to the redox potential value of CO_2 to the formed reduced products (e.g. CH_4/CO_2);
3. effective adsorption of CO_2 or CO_3^{-2} on the surface of the photocatalyst; iv) highly stable photocatalyst [11,12]. **Equations (1) to (8)** present the multistep reactions involved in the reduction of CO_2. As can be seen, the process involves several multiple electron transfer steps, which makes it kinetically difficult to progress. The reduction potentials for photoreduction of CO_2 in the presence of H_2O into several products are given versus NHE at pH=7.0 (Eqs. 1-8):

$CO_2 + \bar{e} \rightarrow C\bar{o}_2^{\cdot}$	E = -1.90V	(1)
$CO_2 + 2H^+ + 2\bar{e} \rightarrow HCOOH$	E = -0.61V	(2)
$CO_2 + 2H^+ + 2\bar{e} \rightarrow CO + H_2O$	E = -0.53V	(3)
$CO_2 + 4H^+ + 4\bar{e} \rightarrow HCHO + H_2O$	E = -0.48V	(4)
$CO_2 + 6H^+ + 6\bar{e} \rightarrow CH_3OH + H_2O$	E = -0.38V	(5)
$CO_2 + 8H^+ + 8\bar{e} \rightarrow CH_4OH + 2H_2O$	E = -0.24V	(6)
$2H^+ + 2\bar{e} \rightarrow H_2$	E = -0.41V	(7)
$2H_2O + 4h^+ \rightarrow O_2 + 4H^+$	E = 0.82V	(8)

One of themost important objectives in CO_2 photoreduction studies is to obtain selective products [13]. Despite so many research activities in this area, selectivity of the product, as well as the conversion efficiency have not been significantly improved. Hence, the research in this area should more focus on providing valuable hydrocarbons and facile separation of the products. For this purpose, extensive understanding of CO_2 reduction mechanism is required; because this process comprises several dependent factors and parameters [14]. The photocatalyst composition, the reductant, and the solvent used in the reaction systemare important factors, which are affecting the products [15]. As observed in **Equations (1) to (8)**, the alteration of the number of electrons and protons can give rise to different products. Correspondingly, to produce CO, the reaction of CO_2 with two protons and two electrons is required, while eight electrons and eight protons are required for producing CH_4 [16]. Another challenge in CO_2 photoreduction reaction is to enhance the efficiency of the reaction. Indeed, rapid recombination of electron/hole ($\bar{e}/h^+$) pairs is a key reason for decreased quantum efficiency. Consequently, fast recombination of these charges and poor light absorption cause low CO_2 conversion efficiency, which limits the practical utilization of the photocatalysts for CO_2 reduction [17,18].

In particular, graphene, known as a single atomic layer of graphite arranged in six-membered rings of carbon atoms, is an expeditiously sparkling rising star on the horizon of materials science. The picturesque honey-comb-like and two-dimensional (2D) sp^2 hybridized graphene has become a hot spot on scientific research due to its extraordinary electrical, mechanical and thermal properties such as excellent mobility of charge carriers (250000 $cm^2/V.s$), large surface area (calculated value = 2630 m^2/g), high thermal conductivity (~5000 W/m.K), optical transparency and good chemical stability [19-21].

Up to now, different approaches have been developed to prepare individual or few layers of graphene sheets by exfoliating graphite flakes. The solution-phase isolation of graphene from graphite, which is the most common route, can be categorized in two different approaches. The first and most regularly used method is the modified Hummer's method using strong oxidizing agents to chemically exfoliate graphite to individual graphene oxide (GO) with abundance of oxygen moieties [22,23]. However, it is widely known that exfoliated GO exemplifies poor electronic conductivity resulting from the interruption of the π system by substitution with a significant amount of defects (oxygen functional groups) [24]. Therefore, various reducing agents such as NaBH4 have been used to reduce GO for the restoration of sp^2 hybridized network [25]. The second approach employs the ultrasonic energy to directly exfoliate graphite in a suitable solvent such as *N,N*-dimethylformamide (DMF) to yield solvent exfoliated graphene (SEG) [26]. Without employing the use of strong oxidizing agents, we developed a facile, low-cost and efficient approach by performing acid pre-treatment for the first time to introduce minimal oxygen-containing groups on the SEG (referred to as acid treated SEG (ATSEG)) for a better interfacial contact with composites. It is anticipated that the electrical mobility of the ATSEG-based nanocomposites with a longer electronic mean free path was enhanced as compared to that of GO-based nanocomposites [27].

Photoassisted CO_2 reduction by H_2 has been frequently reported using materials containing noble or critical metals, such as Pd, Ru and In in its composition [28-31]. For the sake of sustainability, it would be more convenient the use of abundant, non-critical first-raw transition metals in the process, Ni being an obvious candidate considering its availability and the fact that Ni supported on mixed silica alumina (Ni/SiO_2-Al_2O_3) is a commercial catalyst for the thermal CO_2 methanation. CO_2 methanation is one of the few exothermic reactions involving CO_2 as substrate and it can be conveniently carried out in a thermal process using Ni/SiO_2-Al_2O_3 as catalysts at temperatures above 400°C to reach high conversions and rates [32-36]. The advantage of the photoassisted reaction is that it can be performed in the range of temperatures in which the thermal process does not occur or gives only low CO_2 conversions due to the low reaction rates. To shift equilibrium towards the products in an exothermic reaction, low reaction

temperatures, but with adequate rates, are more favorable and this could be reached in the photoassisted process.

Continuing with this line of research, it is of much current interest to find other Ni containing materials that can exhibit even higher activity than Ni/SiO_2-Al_2O_3 for the photoassisted CO_2 reduction by H_2 to CH_4 and to gain information about the mechanism of the photo-assisted process. In the present manuscript, it will be reported that NiO/Ni nanoparticles (NPs) supported on few layers defective graphene (fl-G) is a suitable photocatalyst to promote the photoassisted CO_2 reduction by H_2 with specific rates and quantum yields of about 642 µmol·g/Ni.h and 1.98%, respectively. Graphene (G) is a one-atom thick sheet constituted by sp^2 carbons in hexagonal arrangement. Among the unique properties of G besides their high electric and thermal conductivity, others that important from the catalytic point of view are its high specific surface area (about 2500 m^2/g and its strong interaction with supported metal NPs as consequence of the favorable overlap of the extended π orbital of G with the d orbitals of the metal atoms [37,38]. In addition, G and other 2D related materials have been successfully employed not only as support, but also as additive in catalysts for photocatalytic CO_2 reduction [16,39-42]. It is, therefore, of interest to demonstrate the general ability of graphenes to increase the photocatalytic activity of active components also for other photoassisted CO_2 reductions. In the present manuscript a defective G material obtained by pyrolysis from a natural polysaccharide that contains carbon vacancies, holes and residual oxygenated functional groups was used. Preparation of this type of defective G from alginate has been already reported in the literature and fully characterization is available [43]. It appears that, as it has been well established in semiconducting photocatalysts [44-46]. the presence of graphene results in a remarkable enhancement of the efficiency of Ni to promote the photoassisted process.

Nickel oxide nanostructures were synthesized via solid-state thermal decomposition of $Ni(acac)_2$ nanostructure as precursor that was prepared by sublimation method [47]. Furthermore, NiO/graphene nanocomposite was prepared by the pre-graphenization method that provides a large amount of sites for loading of NiO. Besides, photocatalytic activity of the synthesized NiO/graphene nanocomposite was studied by degradation of methyl orange (MO) as a pollutant. The results of photocatalytic experiments showed that the degradation percentages of MO in existence of the as-prepared nanocomposite under UV and visible light irradiation were about 90.3% after 75 min, and 78% after 180 min, respectively, so this product can be used as an effective photocatalyst [48].

In this study, Photocatalysis for the production of solar fuels and particularly to perform CO_2 reduction to CH_4 with a sufficiently high efficiency depends to the presence of H_2 and absence of H_2O using graphene doped Ni/ NiO nanocomposite.

Materıals and Methods

Materials and Procedures

Alginic acid Na salt from brown algae (Sigma) was pyrolized under Ar atmosphere at 900ºC with a heating rate of 10ºC/min for 2 h to obtain few-layers graphene (fl-G). Ni NPs were deposited by incipient wetness impregnation, adding dropwise a 10 ml Ni (II) chloride hexahydrate solution over preformed fl-G powders under constant stirring. After this time, the Ni(x)-G (x: wt.% Ni) photocatalyst was filtered and washed with mili Q water and acetone until the complete removal of chloride. The solid catalysts were, then, dried overnight in an oven at 80°C. The fl-G powders were reduced under H2 flow (100 ml/min) at 500oC for 2 h with a heating rate of 10ºC/min. The resulting material was dried in a vacuum desiccator at 110oC to remove the remaining H2O and stored under ambient atmosphere before its use as photocatalyst. The amount of Ni present in the samples was determined by inductively coupled plasma-optical emission spectrometry by immersing the catalysts into aqua regia at room temperature for 12 h and analyzing the Ni content of the resulting solution.

Characterization

Powder XRD (X-ray diffraction analysis) patterns were recorded on a Shimadzu XRD-7000 diffractometer using Cu Kα radiation (λ = 1.5418 Å, 40 kV, 40 mA) at a scanning speed of 1° /min in the 10-80° 2θ range. Raman spectrum was collected with a Horiba Jobin Yvon-Labram HR UV-Visible NIR (200-1600 nm) Raman microscope spectrometer, using a laser with the wavelength of 512 nm. The spectrum was collected from 10 scans at a resolution of 2 /cm.

X-Ray Photo Spectroscopy (XPS) spectra were measured on a SPECS spectrometer equipped with a Phoibos 150 9MCD detector using a non-monochromatic X-ray source (Al and Mg) operating at 200 W. The samples were evacuated in the prechamber of the spectrometer at $1x10^{-9}$ mbar. The measured intensity ratios of the components were obtained from the area of the corresponding peaks after nonlinear Shirley-type background subtraction and corrected by the transition function of the spectrometer.

Transmission electron microscopy (TEM) images were recorded in a JEOL JEM 2100F under 200 kV accelerating voltage. Samples were prepared by applying one drop of the suspended material in ethanol onto a carbon-coated copper TEM grid, and allowing them to dry at room temperature.

Diffuse reflectance UV-Vis spectra (DRS) in the range of 200–800 nm were recorded on a Cary 5000 spectrophotometer from Varian.

Photocatalytic tests

A photoreactor (51 ml) with a quartz window and a Ni alloy thermocouple was load with Ni(x)-G photocatalyst. H_2 and CO_2 were introduced in stoichiometric amounts up to achieve a final pressure of 1.3 bar. The photoreactor was heated at different temperatures prior irradiation by means of a heating

mantle equipped with thermocouple and controller, and when the desired temperature was stabilized the photocatalyst was irradiated with a UV-Vis light from a 300 W Xe lamp. Note that the time required before temperature equilibration can be about 30 min. At that moment the lamp is switched on and this is the initial time of the experiments. No change in the gas phase composition was observed at initial reaction time. The CH4 formation was followed by direct measurement of the reactor gases with an Agilent 490 MicroGC having two channels both with TC detectors and Ar as carrier gas. One channel has MolSieve 5A column and analyses H_2, O_2, N_2 and CO. The capability of our Micro GC apparatus to detect CO using Ar as carrier gas has been tested using Abell Linder® steel cylinders containing certified N_2:CO mixtures at different concentrations (20, 10 and 5 vol.%) (Fig. 1). The second channel has a Pore Plot Q column and analyses CO_2, CH_4 and up to C_4 hydrocarbons. Quantification of the percentage of each gas was based on prior calibration of the system injecting mixtures with known percentage of gases.

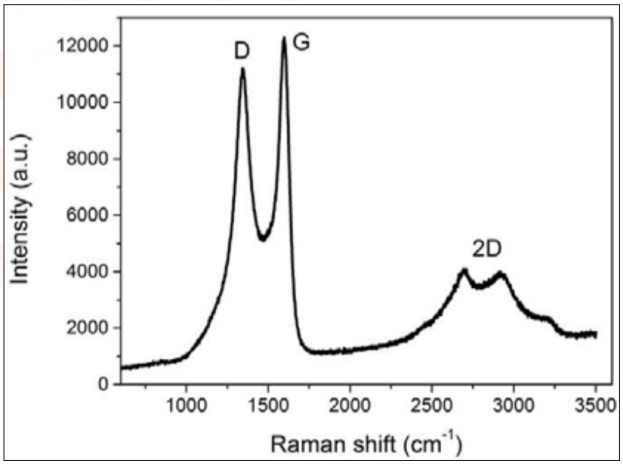

(a)

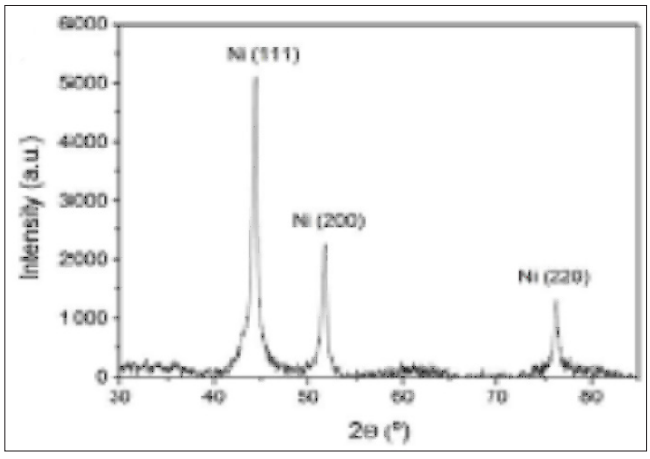

(b)

Figure 1: (a) Raman spectrum of *fl*-G from alginate pyrolysis and subsequent exfoliation recorded upon 512 nm laser excitation (b) XRD pattern of Ni(23)-G photocatalyst.

Preparation of NiO nanoparticles

In this synthesis, NiO nanoparticles were synthesized by the thermal decomposition of Ni(acac)2 nanostructures as a precursor that was prepared via sublimation method. 0.1 g of the precursor was placed in a crucible and was heated up to 500°C for 120 min. Then, the precipitation was cooled to room temperature and the final product was characterized by XRD, Scanning Electron Microscopy (SEM), TEM, Energy dispersive X-ray spectroscopy (EDS) and magnetic properties of the product was investigated by Vibrating sample magnetometer (VSM).

Synthesis of GNS from GO

In this study, the used GO was prepared by a modified Hummers method from natural graphite and reduced through the described method in previous work [49,50].

Preparation of NiO/graphene nanocomposite

The NiO/graphene nanocomposite was synthesized via a pre-graphenization technique. Briefly, 0.1 g from obtained NiO NPs (0.4 mmol) was added to the black suspension of graphene (0.5 mg/ml) and magnetically stirred for 20 min at 90°C. Finally, the above mixture was put in a household microwave oven (Haier, 2450 MHz, 750 W) for 10 min and then it was cooled to room temperature, naturally. Subsequently, the black precipitation was filtered, washed with distilled H_2O and absolute alcohol, and dried at 100°C for 12 h in a vacuum oven. The resulted black powder was collected for the following characterization. The product was characterized by XRD, SEM and UV-vis spectroscopy.

Photocatalytic CO_2 Conversion

In the photocatalytic CO_2 conversion experiment, an empty photoreactor (stainless steel; V = 15.4 cm^3) was purged with CO_2 gas (1000 mg/l in He) and vacuum simultaneously to remove any air or other impurities before and after the loading of the photocatalyst [51]. The photocatalyst (50 mg) was loaded into the photoreactor; moist CO_2 gas (1000 mg/l in He) was passed through a water bubbler, which then enters the photoreactor. The photocatalyst-loaded photoreactor, filled with a mixture of CO_2 and H_2O vapors mixture, was then illuminated by a 100 W Xenon solar simulator (Oriel, LCS-100) with an AM1.5 filter for 1 h, and the reaction products (500 µl) were analyzed using a Shimadzu GC-2014 gas chromatograph (Restek Rt-Q Bond column, ID = 0.53 mm, and length = 30 m) equipped with flame ionization (FID) and thermal conductivity (TCD) detectors. The hournormalized photocatalytic CH4 evolution rate is calculated using Eq. 9.

$$Rate\ of\ CH_4\ evolution = \frac{amount\ of\ CH_4\ produced\ (mg/l)}{amount\ of\ photocatalyst\ used\ (g)} \quad (9)$$

Five cycles of CO_2 photoreduction were performed to test the stability of the same sample; after every test, the photoreactor was purged with Ar gas and vacuum, then re-filled with CO_2 gas (1000 mg/l in He), followed by a 1 h illumination for the next testing cycle.

Results and Discussions

Photocatalyst preparation and characterization

NiO-Ni NPs supported on *fl*-G with different Ni content were prepared adding different amounts of 4 hydrated $NiCl_2$ to *fl*-G dispersions, followed by subsequent thermal reduction of Ni^{+2}

by H_2 atmosphere at 500°C for 2 h. After chemical reductions, the resulting samples were stored under ambient for at least one day before being uses as photocatalyst. This exposure to the ambient can cause some oxidation of the Ni, as it will be discussed below. The Ni content of each sample has been confirmed by ICP-OES elemental analysis. The different samples under study and their respective Ni contents (wt.%) are summarized in Table 1.

Samples	Ni(wt%)[a]	Size (nm)	Total Catalyst amount (mg)	CH_4(µmol/gNi.h
fl-G[a]	-	-	26.12	0
Ni(6)-G	6.61	-	20.17	0
Ni(14)-G	14.42	8.0±2.0	25.40	329.01
Ni(23)-G	23.02	8.5±3.50	40.10	642.68
Ni(23)-G [b]	23.02	8.5±3.52	39.60	0
Ni(23)-G [c]	23.02	8.5±3.56	25.20	0
Ni(26)-G	26.10	13.7±6.0	37.30	303.09
Ni-Al_2O_3/SiO_2	65.30	6.22±1.14[d]	14.40	358.50
NiO	-	< 50	12.73	31.12
NiO-fl-G	23.01		25.41	69.86
Ni(23)-G[f]	23.06	8.5±3.50	25.54	0

a) The difference in weight corresponds to the percentage of graphene;
b) Room temperature;
c) Dark conditions;
d) Photocatalysts pre-activated under H2 atmosphere at 200oC, at 4 h and subsequent reaction at room temperature under light illumination.

Table 1: The Ni content in the NiO/Ni-G samples with Ni average particle size and total catalyst amount. Experimental conditions: at 200°C, at 2240 W/m², at 300 W Xe lamp irradiation, at PH2 = 1.05 bar and at PCO_2 = 0.25 bar, respectively.

Raman spectroscopy was employed to characterize the defective fl-G used as support. The Raman spectrum revealed the typical 2D (2700 /cm), G (1580 /cm) and D (1350 /cm) bands characteristic to the defective G obtained from the pyrolysis of alginate (Fig. 1a). The defects correspond to carbon vacancies and holes generated by evolution of CO_2 and CO during the pyrolysis and to the presence of residual oxygen (about 7 wt.%) remaining from the composition of the polysaccharide precursor after pyrolysis. XRD pattern of the Ni(23)-G photocatalyst revealed that the NiO/Ni NPs were highly crystalline and mainly constituted by Ni metal (Fig. 1b). Diffraction peaks corresponding to NiO, $Ni(OH)_2$ or Ni_2O_3 were undetectable in the diffractogram as can be appreciated in Fig. 1b.

SEM and TEM images of NiO

The SEM image of the as-synthesized NiO is shown in Fig. 2a. In this image, are shown the particles with size about 50 nm. The TEM and Selected area electron diffraction (SAED) images of the NiO NPs are illustrated in Fig. 2b and Fig. 2c, respectively. Uniform NiO NPs with size about 20 nm can be seen in Fig. 2b. The SEAD pattern indicates that the NiO NPs are polycrystalline. They are further indexed as the cubic phase (Fig. 2c). The HRTEM image of the NiO NPs is shown in Fig. 2d. The interplanar spacing is about 0.24 nm, which corresponds to the (1 1 1) plane of the cubic crystalline NiO. Therefore, the HRTEM image further verifies the cubic nature of the synthesized NiO NPs.

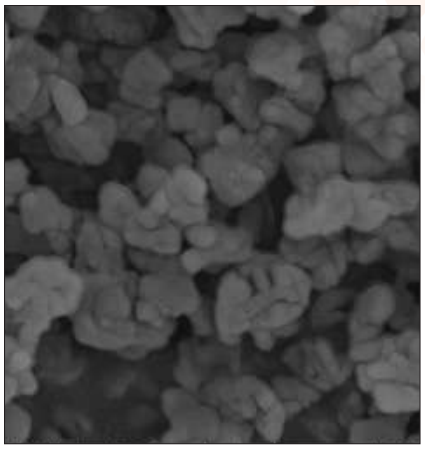

(a)

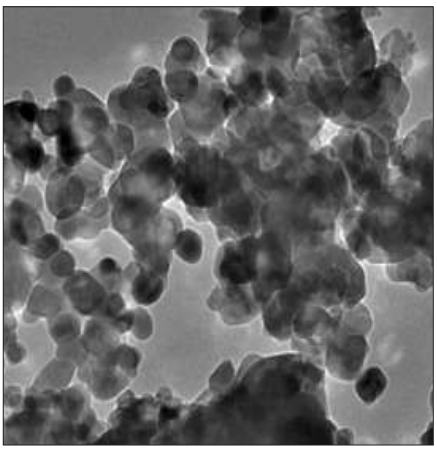

(b)

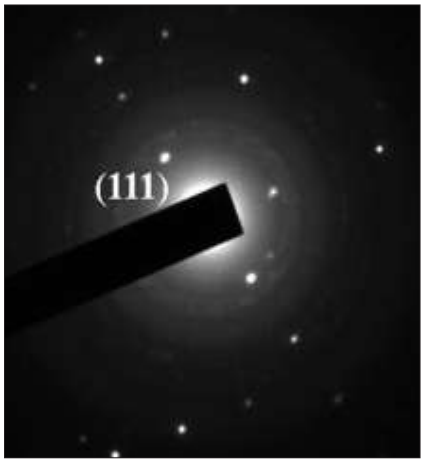

(c)

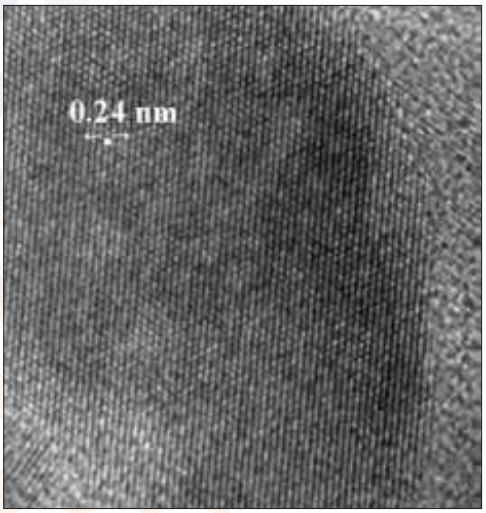

(d)

Figure 2: (a) SEM image of NiO and (b) TEM image of NiO , (c) SAED pattern of NiO and (d) HRTEM image of NiO.

XRD pattern and EDS spectrum of NiO

XRD pattern of NiO NPs is shown in Fig. 3a. It is indexed as a püre cubic structure with according to the literature value (JCPDS card no. 78-0429, Space group: Fm-3m, a = b = c = 4.1771). The crystallite size was estimated using the Scherrer equation is about 30 nm [52]. Fig. 3b shows the EDS microanalysis of the obtained NiO NPs. The Ni and O elements in this spectrum were characterized and there were no peaks, so, the purity of the synthesized NiO NPs was confirmed.

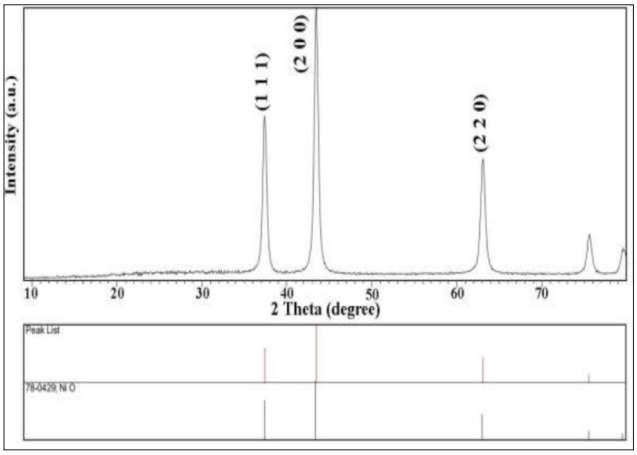

(a)

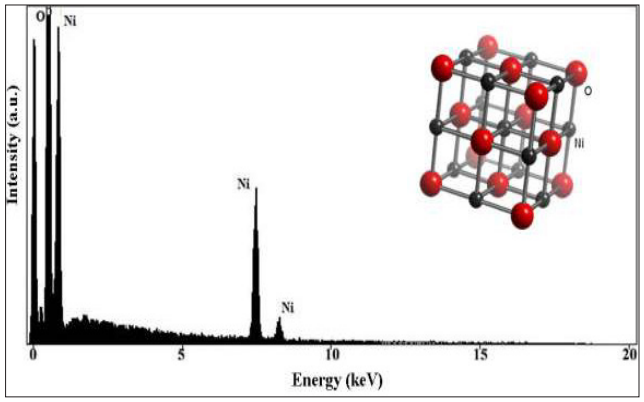

(b)

Figure 3: (a) XRD pattern and (b) EDS spectrum of the obtained NiO.

SEM image and XRD pattern of NiO/graphene nanocomposite

Fig. 4a and Fig. 4b show the low and high magnification FESEM images of the NiO/graphene nanocomposite. From the high magnification image (Fig. 4b), it is clear that the product consists sheet-like structures that NiO NPs (20-30 nm) put on them. The purity of the NiO/graphene nanocomposite was confirmed by X-ray diffraction (XRD) pattern. The diffraction peaks (1 1 1), (2 0 0), (2 2 0), and (3 1 1) in Fig. 4c can be indexed to the cubic phase NiO with space group of Fm/ 3m (JCPDS No. 78-0429) and the broad peak located at 26.5 (0 0 2) corresponds to layered GNS [49]. Presence of NiO crystals in the graphene-based composite was confirmed by the other diffraction peaks in this pattern (Fig. 4c), this result was supported by SEM image and TEM image (Fig. 2a and 2b).

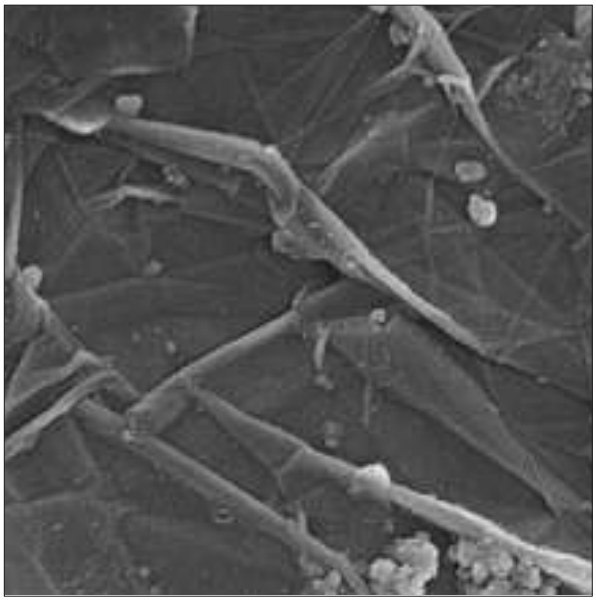

(a)

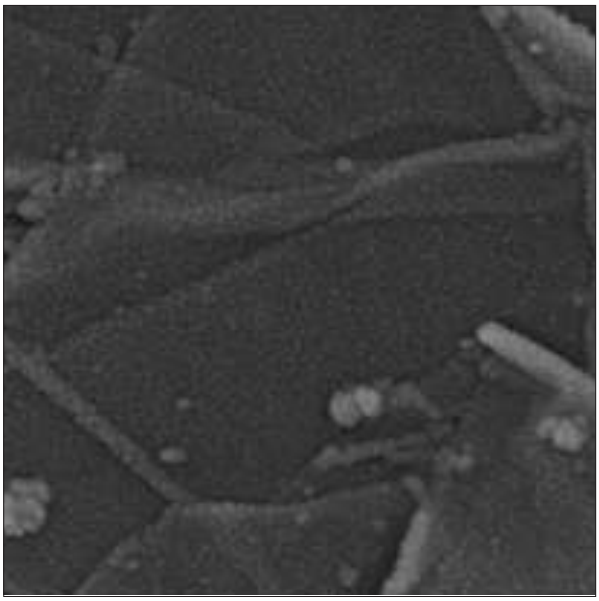

(b)

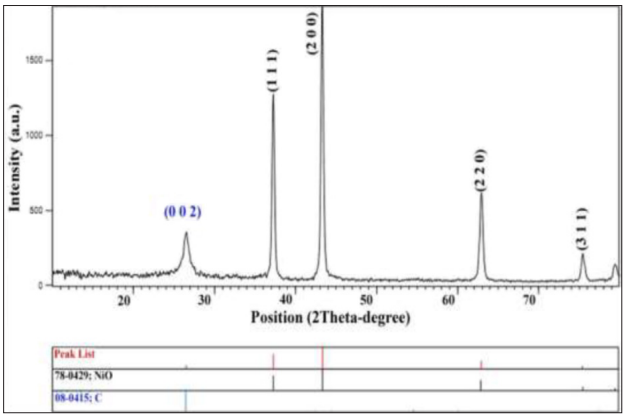

(c)

Figure 4: (a) Low magnification FESEM image, (b) high magnification FESEM image and (c) XRD of the NiO/graphene nanocomposite.

The presence of NiO/Ni NPs on the fl-G sheets was observed by HRTEM and confirmed by FESEM, EDS and elemental mapping (Fig. 5). Fig. 5a corresponds to a representative HRTEM image of NiO/Ni-G showing that NiO/Ni NPs are homogeneously distributed on fl-G sheets. For comparison, an image of *fl*-G sample, prior to Ni deposition, has been also presented as Fig. 5b as well as in Fig. 6. The supported NiO/Ni NPs have a round morphology, as can be observed in the magnified image presented in Fig. 5c, with diameters typically smaller than 10 nm, increasing average particle size with the Ni loading on the G sheet. The histogram corresponding to the particle size distribution for the Ni(23)-G is presented in Fig. 5d. From the measurement of a statistically relevant number of Ni NPs and average particle size of 8.5 ± 3.5 nm was estimated for this sample in spite of the relatively high Ni loading. High-resolution TEM allowed to measure 0.18 nm for particle lattice fringe that corresponds to the interplanar distance of the 200 facets of fcc Ni metal particles thus, confirming that the particles are mainly constituted by Ni^0 [53].

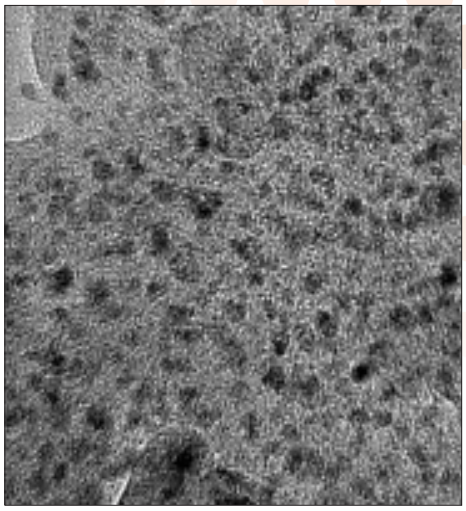

(a)

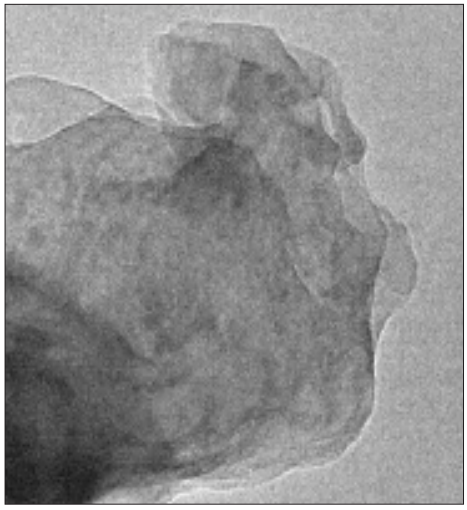

(b)

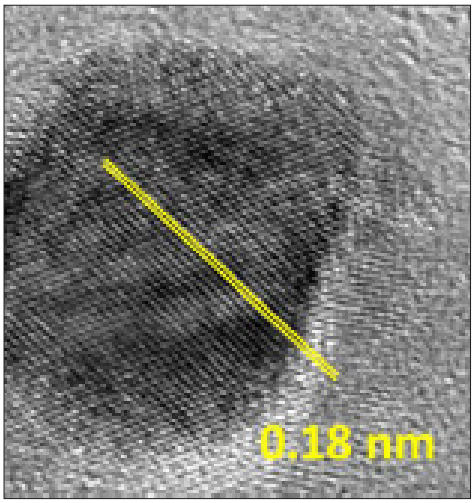

(c)

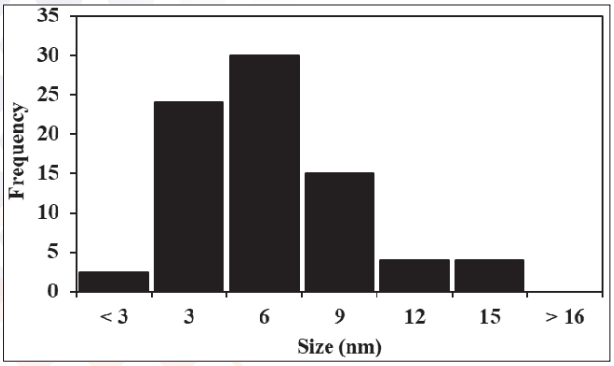

(d)

Figure 5: HRTEM images of (a) Ni(23)-G photocatalyst, (b) fl-G; (c) the NiO/Ni NP and (d) the particle size distribution.

High-resolution XPS peaks of Ni 2p and their corresponding best deconvolution to the different Ni oxidation states are presented in Fig. 6. The Ni 2p3/2 peak shows the presence of two components centered at 853.6 eV and 856.3 eV that can be attributed to Ni^0 and Ni^{+2}, respectively. These binding energies are shifted to higher values compared to those reported in the literature for Ni^0 and Ni^{+2} at 852 and 854 eV, respectively, indicating the occurrence of charge transfer from NiO/Ni NPs as electron donor to G. Previously, a shift to higher binding energy values of 2 eV was also observed for Ni NPs adsorbed on G [54]. Moreover, in the present case, the Ni0 is as a minor component of the experimental XPS Ni 2p3/2 peak. Therefore, in addition to Ni^0 as the predominant phase characterized by XRD, XPS shows the presence of NiO determined by the prominent satellites observed in the Ni 2p3/2 and Ni 2p1/2 peaks. To reconcile both observations, it is worth reminding that while XRD probes the whole sample, XPS only provides information of the outermost nanometers of the metal NPs that are more prone to undergo spontaneous oxidation by exposure to the atmosphere. In addition, XRD is useful characterize crystalline NiO and the presence of NiO as amorphous material due to its thin dimensions would be undetectable by XRD. Therefore, XPS provides two important pieces of information the presence of NiO on the NPs and the charge transfer from NiO/Ni NPs to *fl*-G, implying a notable interaction between them. It should be reminded that even though the preparation of the Ni-G samples was made by H_2 reduction of Ni^{+2}-G at 500°C for 2 h, the samples were stored under ambient conditions and this should lead to a fast passivation of the surface of the Ni NPs with the formation of some NiO overlayers.

The C 1s XPS peak (Fig. 6) shows a major component centered at 284.5 eV corresponding to graphenic sp^2 C, as well as other contributions at 285.5, 286.6 and 289.2 eV corresponding to C atoms bonded to O atoms corresponding to ketones, epoxides and carbonyls groups, respectively. The XPS peak of O 1s (Fig. 6) can be adequately deconvoluted in two main components corresponding to oxygen atoms bonded to C through single or double bonds. The presence of a component at 529.4 eV corresponding to NiO was also observed, although as a minor component [55]. However, the component at 531.1 eV related to $Ni(OH)_2$ could not be identified, confirming NiO as the main oxide component in the Ni 2p3/2 that should form a thin coating on the major metallic Ni NPs [55].

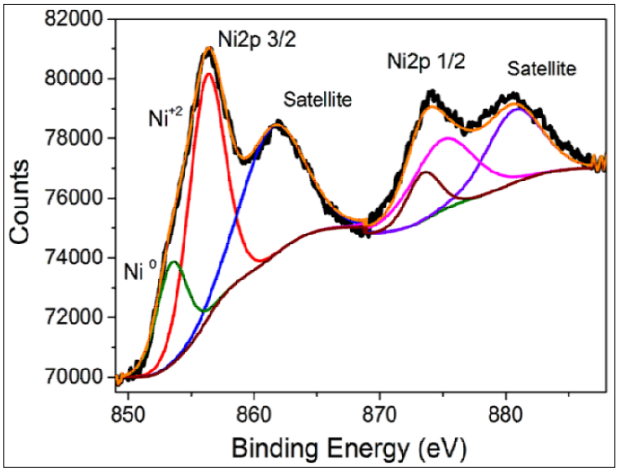

Figure 6: Experimental XPS Ni 2p peaks for the Ni(23)-G sample.

VSM analyses

Magnetization curves of NiO NPs and NiO/graphene nanocomposite at room temperature are shown in Fig. 7a and Fig. 7b, respectively. NiO NPs and NiO/graphene nanocomposite depict a pseudo-single domain and superparamagnetic behavior, respectively, although bulk NiO has now been antiferromagnetic [56]. Pseudo-single domain behavior of NiO and superparamagnetism characteristic of NiO/graphene nanocomposite is confirmed by two signs: The 'S'-shaped curve and low coercivity (Hc = 214.2 Oe for NiO NPs), the saturation magnetization, Ms = 1 emu/g is reached at an applied field of 6000 Oe [57].

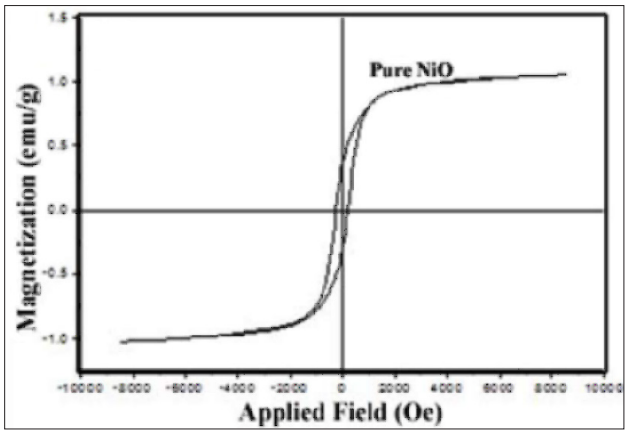

(a)

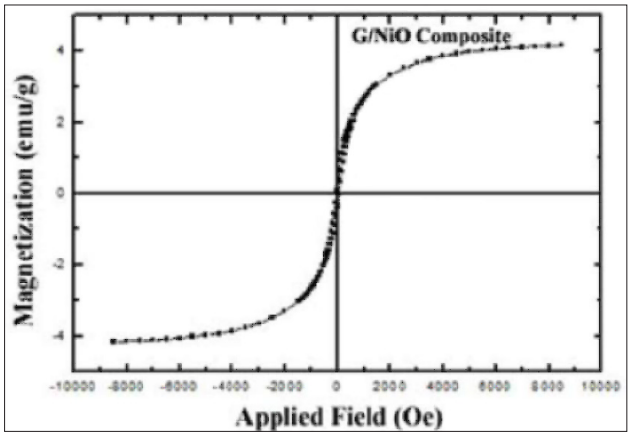

(b)

Figure 7: Magnetization versus applied magnetic field at room temperature for (a) pure NiO nanostructures and (b) NiO/graphene nanocomposite.

Superparamagnetism occurs in NPs, which are single-domain, i.e. composed of a single magnetic domain and this is possible when their diameter is below 50 nm, depending on the materials. When an external magnetic field is applied to an assembly of superparamagnetic NPs, their magnetic moments tend to align along the applied field, leading to a net magnetization. The magnetization curve of the assembly, i.e. the magnetization as a function of the applied field, is a reversible S-shaped increasing function [58]. This change in magnetic property of bulk and NiO NPs and NiO/graphene nanocomposite can be ascribed to finite size effect and unique structure of graphene. With decreasing size of magnetic particles: 1) finite size effect becomes more important and 2) the presence of defects, lattice expansion, broken nature of exchange bonds, and fluctuations in the number of atomic neighbors cause disorder of surface spin and frustration [59].

Recently, extensive studies have been reported about particle size dependent magnetic properties and finite size versus surface effects on magnetic properties of NiO systems have been studied and these investigations show that the strong interplay between finite size effects, surface and interface effects, and defects or oxygen vacancies cause the magnetic properties in NiO become very complex [60-63].

UV–vis absorption spectra

The diffuse reflectance UV-Vis spectra of Ni(23)-G and G samples are shown in Fig. 8a and Fig. 8b. As can be observed there, the only contribution of the Ni NPs in the NiO/Ni-G photocatalyst absorption is in the UV region, below 350 nm [64,65]. NiO should present a prominent band centered at 500 nm, however, in the present case this band could not be detected, thus confirming Ni metal as the principal oxidation state in the NPs as indicated by XRD and that the layer of NiO, detectable only by XPS, has to be thin.

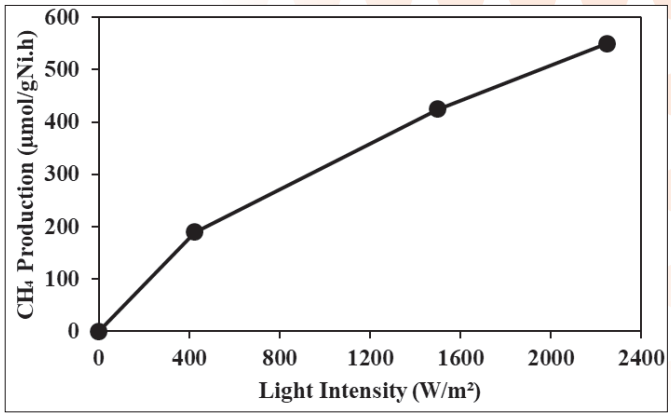

(a)

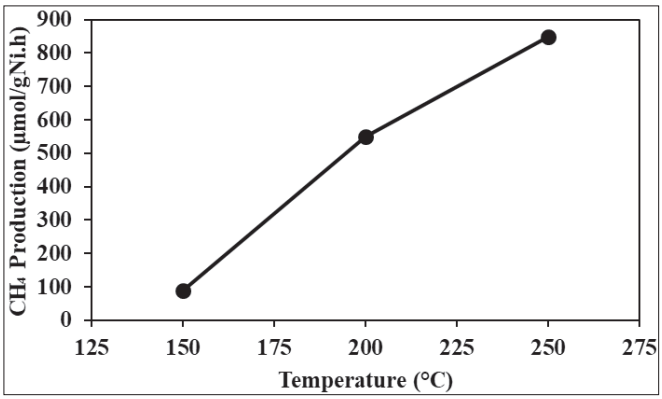

(b)

Figure 8: Specific CH_4 production rate of Ni(23)-G photocatalyst as a function of (a) the light intensity and (b) temperature. Experimental conditions: at total catalyst amount in the light intensity: 25 mg, at total catalyst amount in temperature experiments: 36 mg, at 200°C, at 2240 W/m^2, at PH_2 = 1.05 bar and at PCO_2 = 0.25 bar, respectively.

In Fig. 8, the specific CH_4 production initial rate is clearly dependent of the irradiation power, confirming that, under the present conditions, the CO_2 methanation is a photoassisted process. The apparent quantum yield at 200°C in the photocatalytic CO_2 reduction using the Ni(23)-G photocatalyst was estimated of 1.98 %. On the other hand, the specific CH_4 production initial rate at constant illumination varied also as a function of the reaction temperature. As commented before, reactions performed at room temperature resulted in negligible CH_4 production initial rate (see Table 1). Heating the photoreactor at 150°C resulted in CH_4 evolution rates below 100 µmol/gNi.h. However, temperature of 250°C produced CH_4 at a specific rate of 850 µmol/gNi.h. The dependency of the specific CH4 production rate with the temperature of the system allows us to calculate an apparent activation energy of 38.6 kJ/mol for the process (Fig. 9a and Fig. 9b).

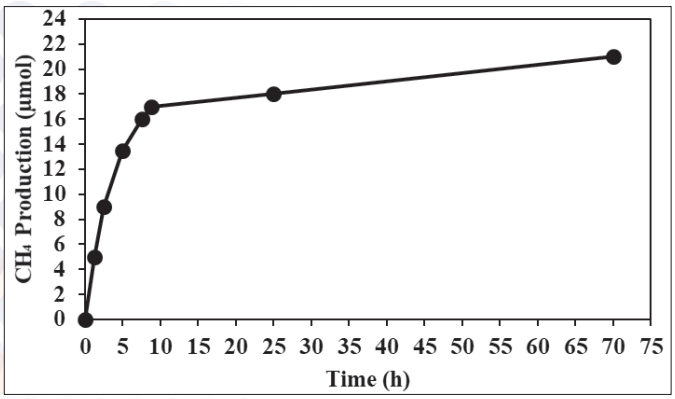

(a)

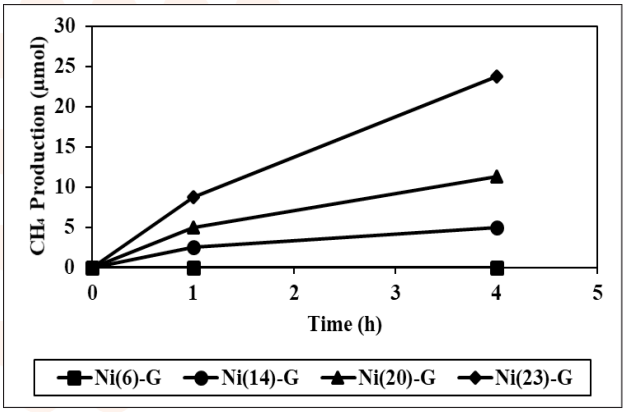

(b)

Figure 9: (a) CH_4 production versus photocatalysis time and (b) CH_4 evolution using the Ni(23)-G photocatalyst. Experimental conditions: at 200°C, at 2240 W/m², at 34.7 mg Ni(23)-G, at PH2 = 1.05 bar and at PCO_2 = 0.25 bar, respectively.

To gain understanding on the mechanism of the photoassisted CO_2 methanation promoted by NiO/Ni-G as photocatalyst and, particularly, the possible role of photogenerated electrons and holes, a series of experiments adding probe molecules were performed. Especifically, a series of photocatalytic tests were carried out adding compounds with increasing ability to act as electron donors. It was assumed that if the mechanism of the photoassisted reaction involves charge separation, the presence of additives that could act as sacrificial electron donor or acceptor agents should enhance or stop, respectively, the photocatalytic activity. Ideally the presence of these electron donor/acceptor additives should not influence the thermal methanation mechanism, at least, in a large extent.

Optical band gap (Eg) may be evaluated based on the optical absorption spectrum using the following Equation [66] (Eq. 10):

$$(Ahv)^n = B(hv - Eg) \quad (10)$$

Where;

hυ : the photon energy,

A : absorbent,

B : a material constant and n is 2 or 1/2 for direct and indirect transitions, respectively.

The optical band gap for the absorption peak is obtained by extrapolating the linear portion of the $(Ahυ)^n$ curve versus hυ to zero. No linear relation was found for n = 1/2, suggesting that the prepared NiO NPs are semiconductors with a direct transition at this energy. The band gap of as-prepared NiO/graphene nanocomposite was calculated about 3.3 eV (Fig. 5d) which is similar to the values reported by other researchers [67,68]. It has a red-shift to that of bulk NiO (3.5 eV) which could be ascribed to the interaction of NiO with graphene backbone and large surface of NiO/graphene nanocomposite [69,70].

Photocatalytic activity and its mechanism

The two mechanisms for photocatalytic activities of pure NiO and NiO/graphene nanocomposite were proposed as follows:

The proposed photocatalytic mechanism for pure NiO NPs (**Equations 11 to 17**):

$$UV + NiO \rightarrow NiO^{\bullet}(h^+ + \bar{e}) \quad (11)$$

$$h^+ + H_20 \rightarrow H^+ + {}^{o}OH \quad (12)$$

$$2h^+ + 2H_20 \rightarrow 2H^+ + H_20_2 \quad (13)$$

$$H_20_2 \rightarrow {}^{o}OH + {}^{o}OH \quad (14)$$

$$\bar{e} + 0_2 \rightarrow {}^{o}\bar{0}_2 \quad (15)$$

$${}^{o}\bar{0}_2 + 20H^{o} + H^+ \rightarrow H_20_2 + 0_2 \quad (16)$$

$$H_20_2 \rightarrow {}^{o}OH + {}^{o}OH \quad (17)$$

The proposed photocatalytic mechanism for NiO/graphene nanocomposite (**Equations 18 to 21**):

$$NiO + hv \rightarrow (\bar{e}_{CB}) + (h^+_{VB}) \rightarrow graphene\ (\bar{e} + h^+) \quad (18)$$

$$NiO\ (\bar{e}_{CB}) + O_{2,ads} \rightarrow {}^{o}\bar{O}_2\ NiO \rightarrow {}^{H20}\ {}^{o}H + NiO \quad (19)$$

$$NiO\ (h^+_{VB}) + OH_{ads\ s} \rightarrow {}^{o}H + NiO \quad (20)$$

$$graphene\ (\bar{e}) + O_{2,ads} \rightarrow {}^{o}\bar{O}_2 + graphene \rightarrow {}^{H20}\ {}^{o}H + graphene \quad (21)$$

Although no changes in the XP spectrum of Ni(23)-G before and after the reaction could be observed, we were interested in ascertain the presence of NiO under the reaction conditions, particularly considering the reductive conditions and the temperature of the methanation. The experimental XPS analysis of Ni(23)-G prior reaction was compared to that measured in situ under the reaction conditions. Thus, a Ni(23)-G sample was submitted to H2 atmosphere at 200oC for 4 h, measuring in situ the Ni 2p peak in the XPS spectrum without exposure to the ambient. As can be observed, the component related to Ni0 (nearly 853 eV) becomes higher under the reaction conditions compared to the sample prior to the reaction. However, the XPS component corresponding to NiO is still bigger than that of the Ni metal. In fact, the relative percentage of Ni0 in the sample before and under *in situ* conditions changed from 15% to 23.5%, respectively. These measurements clearly confirm that in spite of the reductive conditions, the thin layer of NiO should be still present, particularly at initial reaction times that is when the NiO/Ni-G photocatalyst exhibits the highest photocatalytic activity. It can be, therefore, suggested that it is in this outermost part of NiO in contact with Ni where the reaction takes place.

To gain further information on the reaction mechanism and the role of Ni in the process, Ni(23)-G was placed in a sealed

reactor and exposed to a H_2 atmosphere at 200°C for 4 h and then, the sample was allowed to cool down under Ar flow ensuring the complete removal of H_2 gas. Subsequently, the reactor was load only with CO_2 and submitted to the general reaction conditions at 200oC and 2240 W/m² illumination. After 18 h reaction, a detectable amount of CH4 was measured, suggesting the formation of Ni-H species in the first step, without the need of photoactivation that subsequently are able to promote photoassisted CO_2 reduction as reported before [71].

According to these mechanisms, it can be said that graphene layers can postpone the recombination process, so the performance of nanocomposite is better than pure NiO NPs. Furthermore, high surface area, the high separation rate of charge carriers, excellent structure, and great electrical and optical properties of graphene layers of nanocomposite can increase the photocatalytic yield of the graphene-based nanocomposite.

Therefore, the photoassisted CO_2 reduction using Ni(23)-G as promoter was carried out in the presence of dimethylaniline, anisole and p-xylene as electron donors (oxidation potentials of 0.91, 1.93 and 2.18 V vs. Ag/AgCl, respectively) and 4-nitrobenzene as electron acceptor quenchers. Note that according to their boiling points the sacrificial agents are in all cases in the gas phase at the reaction temperature. It was observed that the presence of N,N-dimethylaniline (0.16 mmol) increases the specific CO_2 reduction initial rate by a factor over 2.5, reaching a value of 1600 µmol/gNi.h. CH_4 was also formed in the presence of anisole as electron donor, although at much slower initial reaction rate than in the case of *N,N*-dimethylaniline in accordance with its higher oxidation potential. In contrast, the presence of p-xylene (oxidation potential of 2.18 V vs. Ag/AgCl) completely stopped the production of CH_4, since this aromatic molecule would not be able to quench the holes on Ni(23)-G due to its high oxidation potential (Fig. 10). In the presence of nitrobenzene acting as electron acceptor quencher, CO_2 reduction was also quenched, due to the preferential trapping of electrons by nitrobenzene that has a lower reduction potential compared to CO_2. Note that it would be hard to explain any influence of the presence of electron donor/acceptor quenchers at this small concentration if a photothermal mechanism were operating.

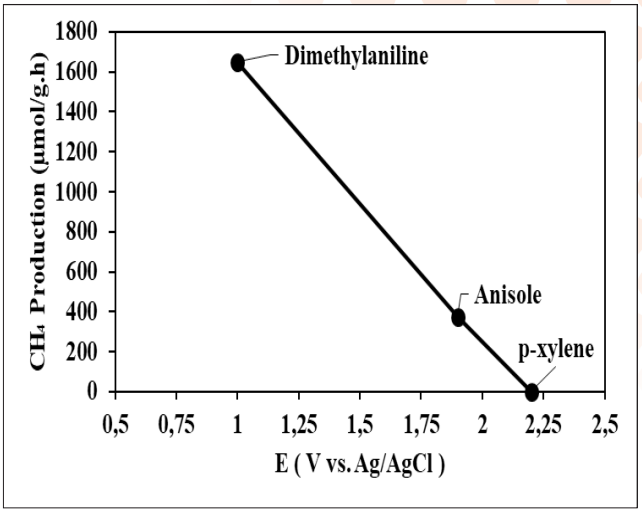

Figure 10: CH_4 production as function of the sacrificial agent oxidation potential. The CH_4 production rate experimental conditions: at 1 h, at 2240 W/m², at 300 W Xenon lamp, at 200°C, at PH_2 = 1.05 bar, at PCO_2 bar and at 20 µl sacrificial agent, respectively.

Transient absorption measurements were carried out to provide support to the generation of charge separation due to the interaction of NiO/Ni NPs and fl-G. Aimed at this purpose, an Ar-purged *fl*-G dispersion in acetonitrile (1 mg/ml) was submitted to 355 nm laser pulse excitation and the transient spectrum was acquired at 30 ns (Fig. 11a). As can be obtained in Fig. 11 the transient spectrum of the fl-G dispersion corresponds to a continuous band decreasing in intensity towards the red part of the spectrum [72]. This behavior has been observed previously in similar graphenic materials and attributed to the charge separation state decaying in microsecond time scale [72]. In a second control, commercial NiO NPs (< 50 nm) from Aldrich were partially reduced in an aqueous N_2H_2 solution (50% vol) to NiO/Ni as determined by XRD in order to simulate the NiO/Ni NPs that are present on the NiO/Ni-G samples, Then, the partially reduced NiO/Ni NPs were dispersed in acetonitrile (1 mg/ml) and the transient spectrum was also acquired upon 355 nm laser excitation (Fig. 11a). A negative signal corresponding to the bleaching of NiO/Ni ground state absorption was observed. Finally, a small aliquot of the dispersed NiO/Ni NPs corresponding to 0.5 mg was added to the fl-G suspension (2 mg) in acetonitrile and the transient spectrum recorded at 30 ns upon 355 nm laser excitation (Fig. 11a). It was observed that addition of NiO/Ni NPs induces quenching of the signal observed for the *fl*-G dispersion, supporting the interaction of the charge separation state of *fl*-G flakes and the NiO/Ni NPs.

The transient signals of the fl-G, NiO/Ni NPs and fl-G containing Ni NPs were monitored at different wavelengths, obtaining for all the wavelength identical results. Fig. 11b shows the kinetics of the transient signal decay of the three samples monitored at 415 nm. As can be observed, the sample containing fl-G presents a transient decay that can be fitted to a single exponential with a lifetime of 36 ns (Fig. 11b).

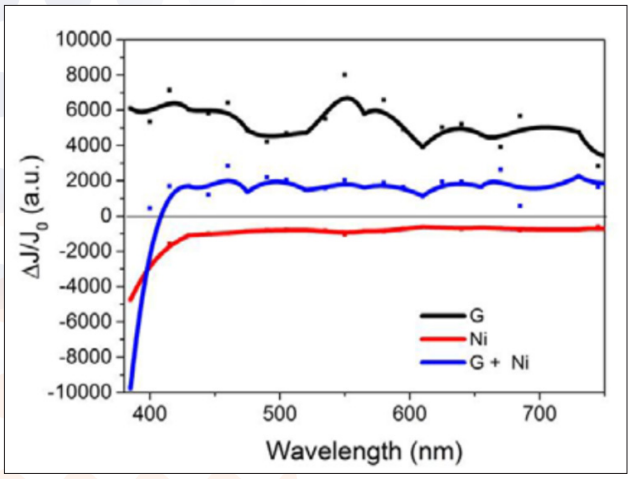

(a)

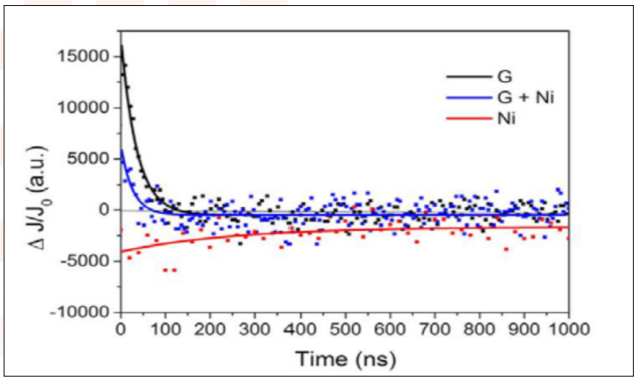

(b)

Figure 11: (a) Transient spectra and (b) kinetics of Ar-purged fl-G (black), NiO/Ni NPs (red) and fl-G with Ni NPs (blue) suspensions. Experimental conditions: at Laser excitation 355 nm, at fl-G acquisition time: 30ns, at fl-G acquisition time: 500 ns and at Transient kinetics: at 415 nm, respectively.

Therefore, to understand the role of the temperature on the photocatalytic process, a series of experiments adding to the reaction vessel small aliquots of H_2O, in the range of the amounts that should be formed in the methanation, were carried out (Fig. 12). It was reasoned that the value of the activation energy determined from the Arrhenius plot of the logarithm of the relative initial reaction rates with the inverse of the absolute temperature is relatively low for a transition state involving bond cleavage, while this value of activation energy is more common for the heat of H_2O desorption from the photocatalyst surface. It should be noted that $H_2{}^{18}O$ formation was detected in the $^{13}C^{18}O_2$ labelled experiments. According to the stoichiometry (Eq. 21), methanation of CO_2 should also produce two H_2O molecules and that at low temperatures these molecules could be preferentially adsorbed on the surface of the photocatalyst, resulting in the inhibition of the reaction.

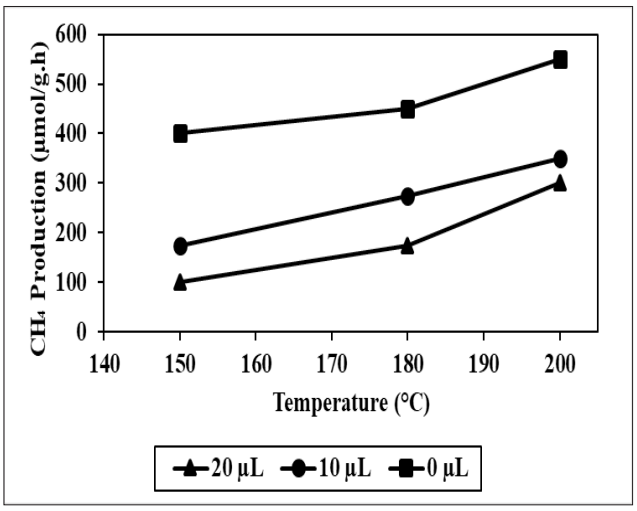

Figure 12: Specific CH_4 production rate measured at different reaction temperatures (a) without or upon (b) the addition of 10 μl of H_2O and (c) the addition of 20 μl of H_2O. Experimental conditions: at 2240 W/m^2, at 25 mg Ni(23)-G catalyst, at PH_2 = 1.05 and at bar, PCO_2 bar, respectively.

In addition of 10 μl H_2O or 20 μl H_2O in the reaction media resulted in a detrimental effect on the specific CH_4 production rate, proportional to the amount of H_2O, the higher the amount of H_2O present at any of the temperatures studied, the lower the specific CH_4 production rate (Fig. 12). However, it is proposed that a possible role of the temperature in the system could be to favor H_2O desorption from the photocatalysts surface, giving an opportunity for H_2 and CO_2 activation. The amount of H_2O formed at final reaction times should correspond to the addition of 890 μl and that the amount of H_2O tested in Fig. 12 is similar to the amount formed at the early stages of methanation. Even with these relatively low H_2O concentrations, their negative influence is already clearly observed in Fig. 12.

Therefore, it is clear that H_2O is a strong poison of the photomethanation and, it is proposed that the role of the temperature is to desorb this generated H_2O acting as poison from the catalyst surface. Finally, the photocatalytic activity of the NiO/Ni-G catalyst was evaluated under continuous flow operation. Continuous flow is very convenient to test photocatalyst stability and the influence of the contact time on the conversion. In the present study, 14.79 ml/min total flow containing, 76.8% N_2, 18.8% H_2 and 4.4% CO_2 was passed through a cylindrical quartz reactor containing 50.7 mg Ni(23)-G photocatalyst loaded on the top of a fritted glass filter inside the reactor. Considering the 0.75 ml photocatalyst volume and the gas flow, the contact time of CO_2 with the irradiated catalysts was 3.1 s. The cylindrical photoreactor was heated at 200°C by means of an electrical heating ribbon controlled with a thermocouple and the irradiation was carried out using the same light source used in the previous experiments, but the light intensity at the photocatalyst was 754.7 W/m^2.

Basic principle of photocatalytic CO_2 reduction

The basic principle of CO_2 reduction with H_2O photocatalysis

occurs when the energy of the photons is enough to promote the electrons (Fig. 8) in the VB to jump to the CB. This occurs in three steps:

- photon absorption and electron–hole pair generation,
- charge separation and migration to surface reaction sites or to recombination sites, and
- surface chemical reactions at the active sites containing donor oxidants at the VB holes and acceptor reductants at the electron center (Fig. 4). Numerous defects associated with these photocatalytic principles have been identified by researchers. During photocatalysis, cation radicals can be produced by injecting charges from an excited molecule into the CB of graphene (Fig. 8) [73].

Irradiation is usually the initial process of CO_2 reduction with H_2O photocatalysis; thus, the excitation of electrons by photons at the ground state is the prerequisite. Periodically, the photoexcitation of electrons at the ground state also occurs in most of the materials adsorbed on the surface of graphene for example, the reaction occurring in dye-sensitized solar cells [74-77]. Different pathways are mainly experienced by the charge carriers. Most individual graphene materials are primarily used for water splitting and oxidation/reduction (Fig. 12) in both suspension and electrode systems [78,79].

As commented above, the photoassisted CO_2 reduction by NiO/Ni-G requires the combination of heating and irradiation to occur. The influence of light intensity and temperature on the photocatalytic CO_2 reduction reaction using Ni(23)-G was, therefore, studied to establish this dependency. The results are presented in Fig. 8.

CO_2 reduction with H_2O

Recently, the increased population as well as industrialization has been detrimental to the environment including the atmosphere [80,81]. Recent increase in CO_2 has remained to be a major issue on this planet [82,83]. CO_2 produced with H_2O from burning fuels from the domestic to industrial level has contributed significantly to the atmospheric air pollution, resulting in the current global warming the world is experiencing [84-87]. There has been an introduction of alternative advanced strategies to cut down the production of CO_2. The SDG 7 has been identified for clean and renewable energy as one of the best mechanisms to reduce the production of CO_2 with H2O in the atmosphere [88,89]. Therefore, due to the increasing demand of fuel and production on the industrial scale, the contribution of CO_2 is still high. Technologies have been developed to reduce the amount of produced CO_2. Among others, the photocatalytic reaction is one of the best technologies for CO_2 reduction (Fig. 13) [50].

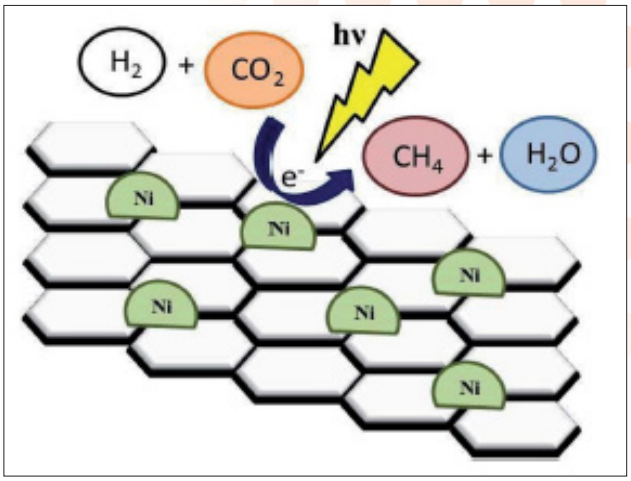

Figure 13: The photoreduction of CO_2 with H_2O to CO.

In order to confirm the origin of the C source in the CH_4 production and the formation of H_2O according to Eq. 22 $^{13}C^{18}O_2$ was used as substrate and the obtained products were analyzed after 2 h reaction under optimal conditions by GC-MS spectroscopy (Fig. 10).

$$CO_2 + 4H_2 \rightarrow CH_4 + 2H_2O \quad \Delta G = -115 \text{ KJ / } mol \qquad (22)$$

The analysis shows a mix of 14% of unlabeled $^{12}CH_4$ and 86% of $^{13}CH_4$, indicating that a minor portion of the produced CH_4 does not come from the labelled substrate. The most likely origin of the unlabeled CH_4 should be the C atoms of *fl*-G. In order to confirm this hypothesis a stability experiment was performed submitting Ni(23)-G sample at reaction conditions (200°C and 2240 W/m^2) under Ar atmosphere, and measuring the CO_2 evolution (Fig. 11). As can be observed a small amount of CO_2 was observed to evolve under these conditions for the first 20 h. After this period, the CO_2 amount remained constant, confirming, on the one hand, the presence of small amounts of CO_2 originated from *fl*-G and, on the other hand, that the photocatalyst is photostable at long reaction times. It should be, however, reminded that the blank experiment with *fl*-G in where formation of CH_4 was not observed, indicates that even for this contribution of unlabeled CH_4, the presence of NiO/Ni is needed. In the same experiment using $^{13}C^{18}O_2$, observation of $H_2{}^{18}O$ was also detected (Fig. 10), confirming the formation of H_2O in the methanation. CH_4 production efficiencies was showed for different N/NiO-graphene nanocomposites ratios during photocatalysis process in Table 2. 99% maximum CH_4 production efficieny was measured at Ni/NiO(23)-G nanocomposite after CO_2 reduction during photocatalysis process, at 200°C, at 2240 W/m^2, at 300 W Xe lamp irradiation, at P_{H2} = 1.05 bar and PCO2 = 0.25 bar, respectively (Table 2).

Samples	CH_4 production (%)	Samples	CH_4 production (%)	Samples	CH_4 production (%)
Ni(6)-G	5	NiO(6)-G	13	Ni/NiO(6)-G	24
Ni(10)-G	7.5	NiO(10)-G	21	Ni/NiO(10)-G	40
Ni(14)-G	10	NiO(14)-G	30	Ni/NiO(14)-G	61
Ni(20)-G	18	NiO(20)-G	42	Ni/NiO(20)-G	85
Ni(23)-G	25	NiO(23)-G	53	Ni/NiO(23)-G	99

Table 2: CH_4 production efficiencies at different Ni/NiO-graphene (G) nanocompoasite samples, at 200°C, at 2240 W/m^2, at 300 W Xe lamp irradiation, at P_{H2} = 1.05 bar and PCO_2 = 0.25 bar, respectively.

Zhou and co-workers described the facile in situ synthesis of a graphene (g-C_3N_4)–N-TiO_2 heterojunction as a competent photocatalyst for the selective photoreduction of CO_2 with H_2O to CO. The composites of graphene, i.e., carbon nitride and N2-doped TiO2 composites (g-C_3N_4–N-TiO_2) were in situ synthesized by the thermal treatment of well-mixed urea and $Ti(OH)_4$ in an alumina crucible with a cover at different mass ratios. These results prove that graphene has high photocatalytic CO_2 reduction with H_2O as compared to its precursors [90].

Photo-assisted CO_2 reduction with H_2O by H_2 has been repeatedly described using fabrics covering noble or analytical metals, such as Pd, Ru and In [28-31,91,92]. It was found that H_2O formed in the photocatalytic reaction of NiO/Ni NPs supported on defective graphene via photo-assisted CO_2 reduction with H_2 has a negative influence on the photocatalytic activity and studies further confirmed that H_2O desorption is one of the reasons why the system requires heating [93]. Therefore, it is anticipated that a promising function of temperature in the system can be to promote H_2O desorption from the photocatalyst surface, providing an opportunity for H_2 and CO_2 activation [36,38].

Conclusıon

The preparation of NiO/graphene nanocomposite can help to delay the recombination process, so the photocatalytic performance improves. Hence, NiO/graphene nanocomposite was identified as an effective adsorbent and photocatalyst in waste-water treatment because of it shows an excellent performance to remove pollutants, rapidly.

Finally, in the present study, it has been shown that NiO/Ni NPs supported on *fl*-G is a suitable photocatalyst to perform methanation of CO_2 at temperatures about 200°C, reaching specific CH_4 formation rates of 642 µmol/gNi.h that are about double than that measured for Ni NPs supported on high surface area silica-alumina and apparent quantum yields of 1.98%. 99% maximum CH_4 production efficieny was measured at Ni/NiO(23)-G nanocomposite after CO_2 reduction during photocatalysis process, at 200°C, at 2240 W/m^2, at 300 W Xe lamp irradiation, at P_{H2} = 1.05 bar and PCO_2 = 0.25 bar, respectively.

In addition to, the positive effect of graphene appears to be due to the photoinduced electron transfer from excited NiO/Ni NPs to the graphene sheet. Experimental evidence indicates that the role of the temperature is to desorb H_2O formed also in the process, causing apparent deactivation of the photocatalyst. Under optimal conditions and under continuous flow, photocatalyst deactivation was reduced probably to the more favorable H_2O removal. Mechanistic data using electron donor, acceptor quenchers and observation of *fl*-G charge separated stated quenching by NiO/Ni NPs support that the reaction mechanism involves photogenerated charge separation derived from photon absorption in the UV region.

Acknowledgements

This research study was undertaken in the Environmental Microbiology Laboratury at Dokuz Eylul University Engineering Faculty Environmental Engineering Department, Izmir, Turkey.

References

1. Hu B, Guild C, Suib SL (2013) Thermal, electrochemical, and photochemical conversion of CO_2 to fuels and value-added products. J CO_2 Util 1: 18-27.
2. Maeda C, Miyazaki Y, Ema T (2014) Recent progress in catalytic conversions of carbon dioxide. Catal Sci Technol 4: 1482-1497.
3. Park SM, Razzaq A, Park YH, Sorcar S, Park Y, et al. (2016) Hybrid CuxO−TiO_2 Heterostructured composites for photocatalytic CO_2 reduction into methane using solar ırradiation: sunlight into fuel. American Chemical Society (ACS) Publications Omega 1: 868-875.
4. Habisreutinger SN, Schmidt-Mende L, Stolarczyk JK (2013) Photocatalytic Reduction of CO_2 on TiO_2 and Other Semiconductors. Angew Chem Int Ed 52: 7372-7408.
5. Huang C, Li Z, Zou ZA (2016) Perspective on Perovskite Oxide Semiconductor Catalysts for Gas Phase Photoreduction of Carbon Dioxide. MRS Commun 6: 216-225.
6. Ran J, Jaroniec M, Qiao SZ (2018) Cocatalysts in Semiconductor-based Photocatalytic CO_2 Reduction: Achievements, Challenges, and Opportunities. Adv Mate 30: 1704649-1704680.
7. El-Khouly ME, El-Mohsnawy E, Fukuzumi S (2017) Solar Energy Conversion: from Natural to Artificial Photosynthesis. J Photochem Photobiol C Photochem Rev 31: 36-83.
8. Takeda H, Ishitani O (2010) Development of Efficient Photocatalytic Systems for CO_2 Reduction Using Mononuclear and Multinuclear Metal Complexes Based on Mechanistic Studies. Coord Chem Rev 254: 346-354.
9. Liu X, Inagaki S, Gong J (2016) Heterogeneous Molecular Systems for Photocatalytic CO_2 Reduction with Water Oxidation. Angew Chem Int Ed 55: 14924-14950.

10. Hong J, Zhang W, Ren J, Xu R (2013) Photocatalytic Reduction of CO_2: A Brief Review on Product Analysis and Systematic Methods. Anal Methods 5: 1086-1097.
11. Fan W, Zhang Q, Wang Y (2013) Semiconductor-based Nanocomposites for Photocatalytic H_2 Production and CO_2 Conversion. Phys Chem Chem Phys 15: 2632-2649.
12. Mao J, Li K, Peng T (2013) Recent Advances in the Photocatalytic CO_2 Reduction over Semiconductors. Catal Sci Technol 3: 2481-2498.
13. Yin S, Han J, Zhou T, Xu R (2015) Recent Progress in g-C3N4 Based Low Cost Photocatalytic System: Activity Enhancement and Emerging Applications. Catal Sci Technol 5: 5048-5061.
14. Chang X, Wang T, Gong J (2016) CO_2 Photo-reduction: Insights into CO_2 Activation and Reaction on Surfaces of Photocatalysts. Energy Environ Sci 9: 2177-2196.
15. Dasab S, Wan Daud WMA (2014) A Review on Advances in Photocatalysts Towards CO_2 Conversion. RSC Adv 4: 20856-20893.
16. Kou J, Lu C, Wang J, Chen Y, Xu Z, et al. (2017). Selectivity Enhancement in Heterogeneous Photocatalytic Transformations. Chem Rev 117: 1445-1514.
17. Low J, Yu J, Ho W (2015) Graphene-Based Photocatalysts for CO_2 Reduction to Solar Fuel, The Journal of Physical Chemistry Letters 6: 4244-4251.
18. Akhundi A, Habibi-Yangjeh A, Abitorabi M, Pouran SR (2019) Review on photocatalytic conversion of carbon dioxide to value-added compounds and renewable fuels by graphitic carbon nitride-based photocatalysts, Catalysis Reviews 61: 595-628.
19. Park S, Ruoff RS (2009) Chemical methods for the production of graphenes. Nat Nanotechnol 4: 217-224.
20. Geim AK (2009) Graphene: Status and prospects. Science 324: 1530-1534.
21. Shen J, Shi M, Yan B, Ma H, Li N, Ye M (2011) Ionic liquid-assisted one-step hydrothermal synthesis of TiO_2-reduced graphene oxide composites. Nano Res 4: 795-806.
22. Chen C, Cai W, Long M, Zhou B, Wu Y, et al. (2010) Synthesis of visible-light responsive graphene oxide/ TiO2composites with p/n heterojunction. ACS Nano 4: 6425-6432.
23. Li Q, Guo B, Yu J, Ran J, Zhang B, et al. (2011) Highly efficient visible-light-driven photocatalytic hydrogen production of CdS-cluster-decorated graphene nanosheets. J Am Chem Soc 133: 10878-10884.
24. Perera SD, Mariano RG, Vu K, Nour N, Seitz O, *et al.* (2012) Hydrothermal synthesis of graphene-TiO2 nanotube composites with enhanced photocatalytic activity. ACS Catal 2: 949-956.
25. Shin HJ, Kim KK, Benayad A, Yoon SM, Park HK, *et al.* (2009) Efficient reduction of graphite oxide by sodium borohydride and its effect on electrical conductance. Adv Funct Mater 19: 1987-1992.
26. Liang YT, Vijayan BK, Gray KA, Hersam MC (2011) Minimizing graphene defects enhances titania nanocomposite-based photocatalytic reduction of CO_2 for improved solar fuel production. Nano Lett 11: 2865-2870.
27. Ong WJ, Tan LL, Chai SP, Yong ST, Mohamed AR (1998) Self-Assembly of Nitrogen-Doped $TiO_2$with Exposed {001} Facets on the Graphene Scaffold as Photo-Active Hybrid Nanostructures for Reduction of Carbon Dioxide to Methane, Nano Research 20-44.
28. O'Brien PG, Sandhel A, Wood TE, Jelle AA, Hoch LB, et al. (2014). Photomethanation of Gaseous CO_2 over Ru/ Silicon Nanowire Catalysts with Visible and Near-Infrared Photons, Advanced Science 1: 1400001.
29. Li M, Li P, Chang K, Wang T, Liu L, et al. (2015) Highly efficient and stable photocatalytic reduction of CO_2 to CH_4 over Ru loaded $NaTaO_3$, Chemical Communications 51: 7645-7648.
30. Ghuman KK, Hoch LB, Szymanski P, Loh JYY, Kherani NP, et al. (2016) Photoexcited Surface Frustrated Lewis Pairs for Heterogeneous Photocatalytic CO_2 Reduction, Journal of the American Chemical Society 138: 1206-1214.
31. Ren J, Ouyang S, Xu H, Meng X, Wang T, *et al*. (2017) Targeting Activation of CO_2 and H-2 over Ru-Loaded Ultrathin Layered Double Hydroxides to Achieve Efficient Photothermal CO_2 Methanation in Flow-Type System, Adv Energy Mater 7: 1601657.
32. Inui T, Funabiki M, Suehiro M, Sezume T (1979) Methanation of CO_2 and CO on supported nickel-based composite catalysts, Journal of the Chemical Society-Faraday Transactions I 75: 787-802.
33. Du G, Lim S, Yang Y, Wang C, Pfefferle L, et al. (2007) Methanation of carbon dioxide on Ni-incorporated MCM-41 catalysts: The influence of catalyst pretreatment and study of steady-state reaction, Journal of Catalysis 249: 370-379.
34. Pan YX, Liu CJ, Ge Q (2010) Effect of surface hydroxyls on selective CO_2 hydrogenation over Ni-4/gamma-Al2O3: A density functional theory study, Journal of Catalysis 27: 227-234.
35. Abello S, Berrueco C, Montane D (2013) High-loaded nickel-alumina catalyst for direct CO2 hydrogenation into synthetic natural gas (SNG), Fuel 113: 598-609.
36. Frontera P, Macario A, Ferraro M, Antonucci P (2017) Supported Catalysts for CO_2 Methanation: A Review Catalysts 7: 59-87.
37. Rao CNR, Sood AK, Subrahmanyam KS, Govindaraj A (2009) Graphene: The New Two-Dimensional Nanomaterial, Angewandte Chemie International Edition 48: 7752-7777.
38. Mateo D, Esteve-Adell I, Albero J, Primo A, García H (2017) Oriented 2.0.0 Cu_2O nanoplatelets supported on few-layers graphene as efficient visible light photocatalyst for overall water splitting, Applied Catalysis B: Environmental 201: 582-590.
39. Wang K, Li Q, Liu B, Cheng B, Ho W, et al. (2015) Sulfur-doped g-C_3N_4 with enhanced photocatalytic CO_2-reduction performance, Applied Catalysis B: Environmental 176: 44-52.
40. Gusain R, Kumar P, Sharma OP, Jain SL, Khatri OP (2016) Reduced graphene oxide–CuO nanocomposites for photocatalytic conversion of CO_2 into methanol

under visible light irradiation, Applied Catalysis B: Environmental 181: 352-362.
41. Kumar P, Joshi C, Barras A, Sieber B, Addad A, et al. (2017) Core–shell structured reduced graphene oxide wrapped magnetically separable rGO@CuZnO@Fe_3O_4 microspheres as superior photocatalyst for CO2 reduction under visible light, Applied Catalysis B: Environmental 205: 654-665.
42. Nikokavoura A, Trapalis C (2017) Alternative photocatalysts to TiO_2 for the photocatalytic reduction of CO_2, Applied Surface Science 391: 149-174.
43. Primo A, Atienzar P, Sanchez E, Delgado JM, Garcia H (2012) From biomass wastes to large-area, high-quality, N-doped graphene: catalyst-free carbonization of chitosan coatings on arbitrary substrates, Chemical Communications 48: 9254-9256.
44. Williams G, Seger B, Kamat PV (2008) TiO_2-graphene nanocomposites. UV-assisted photocatalytic reduction of graphene oxide, Acs Nano 2: 1487-1491.
45. Zhang H, Lv X, Li Y, Wang Y, Li J (2010) P25-Graphene Composite as a High Performance Photocatalyst, Acs Nano 4: 380-386.
46. Xiang Q, Yu J, Jaroniec M (2012) Graphene-based semiconductor photocatalysts, Chemical Society Reviews 41: 782-796.
47. Faezeh Soofivand F, Masoud Salavati-Niasari M (2017) Step synthesis and photocatalytic activity of NiO/graphene nanocomposite under UV and visible light as an effective photocatalyst, Journal of Photochemistry and Photobiology A: Chemistry 337: 44-53.
48. Hummers WS, Offeman RE (1958) Preparation of graphitic oxide, Journal of the American Chemical Society 80: 1339-1339.
49. Chen CM, Zhang Q, Huang JQ, Zhang W, Zhao XC, et al. (2012) Chemically derived graphene–metal oxide hybrids as electrodes for electrochemical energy storage: pre-graphenization or post-graphenization?, Journal of Materials Chemistry 22: 13947-13955.
50. He Y, Zhang L, Fan M, Wang X, Walbridge ML, et al. (2015) Z-scheme SnO_2_x/g-C_3N_4 composite as an efficient photocatalyst for dye degradation and photocatalytic CO2 reduction, Sol Energy Mater Sol Cells 137: 175-184.
51. Kim HR, Razzaq A, Heo HJ, In SI (2013) Photocatalytic conversion of CO_2 into hydrocarbon fuels with standard titania (degussa P25) using newly installed experimental setup. Rapid Commun Photosci 2: 64-66.
52. Oh WC, Zhang FJ, Chen ML (2010) Characterization and photodegradation characteristics of organic dye for Pt–titania combined multi-walled carbon nanotube composite catalysts, Journal of industrial and engineering chemistry 16: 321-326.
53. Singh MK, Agarwal A, Gopal R, Swarnkar RK, Kotnala RK (2011) Dumbbell shaped nickel nanocrystals synthesized by a laser induced fragmentation method, Journal of Materials Chemistry 21: 11074-11079.
54. Blandez JF, Esteve-Adell I, Primo A, Alvaro M, García H (2016) Nickel nanoparticles supported on graphene as catalysts for aldehyde hydrosilylation, Journal of Molecular Catalysis A: Chemical 412: 13-19.
55. Biesinger MC, Payne BP, Lau LWM, Gerson A, Smart RSC (2009) X-ray photoelectron spectroscopic chemical state quantification of mixed nickel metal, oxide and hydroxide systems, Surface and Interface Analysis 41: 324-332.
56. Ngo A, Bonville P, Pileni M (1999) Nanoparticles of: Synthesis and superparamagnetic properties, The European Physical Journal B-Condensed Matter and Complex Systems 9: 583-592.
57. Khadar MA, Biju V, Inoue A (2003) Effect of finite size on the magnetization behavior of nanostructured nickel oxide, Materials research bulletin 38: 1341-1349.
58. Néel L (1952) Théorie du traînage magnétique de diffusion, Journal de Physique et le Radium 13: 249-264.
59. Kisan B, Shyni P, Layek S, Verma H, Hesp D, et al. (2014) Finite size effects in magnetic and optical properties of antiferromagnetic NiO nanoparticles, Magnetics, IEEE Transactions on 50: 1-4.
60. Tiwari, S. and Rajeev, K. (2005). Signatures of spin-glass freezing in NiO nanoparticles, Physical Review B, 72, 104433.
61. Li, L., Chen, L., Qihe, R. and Li, G. (2006). Magnetic crossover of NiO nanocrystals at room temperature, Applied physics letters, 89, 134102.
62. Peck, M., Huh, Y., Skomski, R., Zhang, R., Kharel, P., Allison, M., Sellmyer, D. and Langell, M. (2011). Magnetic properties of NiO and (Ni, Zn) O nanoclusters, Journal of Applied Physics, 109, 07B518.
63. Mandal, S., Menon, K.S., Mahatha, S. and Banerjee, S. (2011). Finite size versus surface effects on magnetic properties of antiferromagnetic particles, Applied Physics Letters, 99, 232507.
64. Mahfouz R, Cadete Santos Aires FJ, Brenier A, Jacquier B, Bertolini JC (2008) Synthesis and physico-chemical characteristics of nanosized particles produced by laser ablation of a nickel target in water, Applied Surface Science 254: 5181-5190.
65. Elango G, Roopan SM, Dhamodaran KI, Elumalai K, Al-Dhabi NA, Arasu MV (2016) Spectroscopic investigation of biosynthesized nickel nanoparticles and its larvicidal, pesticidal activities, Journal of Photochemistry and Photobiology B: Biology 162: 162-167.
66. Hagfeldt A, Graetzel M (1995) Light-induced redox reactions in nanocrystalline systems, Chemical Reviews 95: 49-68.
67. Salavati-Niasari M, Davar F, Fereshteh Z (2010a) Synthesis of nickel and nickel oxide nanoparticles via heattreatment of simple octanoate precursor, Journal of alloys and Compounds 494: 410-414.
68. Salavati-Niasari M, Mir N, Davar F (2010b) A novel precursor in preparation and characterization of nickel oxide nanoparticles via thermal decomposition approach, Journal of Alloys and Compounds 493: 163-168.
69. Xu Y, Schoonen MA (2000) The absolute energy positions of conduction and valence bands of selected semiconducting minerals, American Mineralogist 85: 543-556.
70. Liu Q, Liu Z, Zhang X, Yang L, Zhang N, et al. (2009)

Polymer photovoltaic cells based on solution-processable graphene and P3HT, Advanced Functional Materials 19: 894-904.
71. Sastre F, Puga AV, Liu L, Corma A, García H (2014) Complete Photocatalytic Reduction of CO_2 to Methane by H_2 under Solar Light Irradiation, Journal of the American Chemical Society 136: 6798-6801.
72. Baldoví HG, Álvaro M, Ferrer B, García H (2016) Photoinduced Charge Separation on the Microsecond Timescale in Graphene Oxide and Reduced Graphene Oxide Suspensions, ChemPhysChem 17: 958-962.
73. Nasr C, Vinodgopal K, Fisher L, Hotchandani S, Chattopadhyay AK, et al. (1996) Environmental photochemistry on semiconductor surfaces. Visible light induced degradation of a textile diazo dye, naphthol blue black, on TiO2 nanoparticles, J Phys Chem 100: 8436-8442.
74. Nosaka Y, Nosaka AY (2017) Generation and Detection of Reactive Oxygen Species in Photocatalysis, Chem. Rev 117: 11302-11336.
75. Adormaa BB, Darkwah WK, Ao Y (2018) Oxygen vacancies of the TiO_2 nano-based composite photocatalysts in visible light responsive photocatalysis, RSC Adv 8: 33551.
76. Li T, Zhao L, He Y, Cai J, Luo M, et al. (2013) Synthesis of g-C_3N_4/$SmVO_4$ composite photocatalyst with improved visible light photocatalytic activities in RhB degradation, Appl Catal B 129: 255-263.
77. Hollmann D, Karnahl M, Tschierlei S, Kailasam K, Schneider M, et al. (2014) Structure-Activity Relationships in Bulk Polymeric and Sol–Gel-Derived Carbon Nitrides during Photocatalytic Hydrogen Production, Chem. Mater 26: 1727-1733.
78. Nakamura I, Negishi N, Kutsuna S, Ihara T, Sugihara S, et al. (2000) Role of oxygen vacancy in the plasmatreated TiO photocatalyst with visible light activity for NO removal, J Mol Catal A: Chem 161: 205-212.
79. Gholipour MR, Dinh CT, B´elandb F, Do TO (2015) Nanocomposite heterojunctions as sunlight-driven photocatalysts for hydrogen production from water splitting, Nanoscale, 7: 8187-8208.
80. Manahan SE (2000) The endangered Global Atmosphere, in Environmental Chemistry, Lewis Publisher, Boca Raton, Landon, New York, Washington D.C, 7th edn.
81. Darkwah WK, Oswald KA (2019) Photocatalytic Applications of Heterostructure Graphitic Carbon Nitride: Pollutant Degradation, Hydrogen Gas Production (water splitting), and CO_2 Reduction, Nanoscale Res Lett.
82. Chakravarty S, Chikkatur A, de Coninck H, Pacala S, Socolow R, et al. (2009) Sharing global CO_2 emission reductions among one billion high emitters, Proc Natl Acad Sci U S A 106: 11884-11888.
83. Rogelj J, Luderer G, Pietzcker RC, Kriegler E, Schaeffer M, *et al*. (2015) Energy system transformations for limiting end-of-century warming to below 1.5°C, Nat Clim Change 5: 519-527.
84. Duguma LA, Minang PA, Van Noordwijk M (2014) Climate Change Mitigation and Adaptation in the Land Use Sector: From Complementarity to Synergy, Environ Manage 54: 420-432.
85. Yu W, Xu D, Peng T (2015) Enhanced photocatalytic activity of g-C_3N_4 for selective CO_2 reduction to CH_3OH via facile coupling of ZnO: A direct Z-scheme mechanism, J Mater Chem A 3: 19936-19947.
86. Solano Rodriguez B, Drummond P, Ekins P (2017) Decarbonizing the EU energy system by 2050: an important role for BECCS, Clim Pol 17: 93-110.
87. Xu Y, Ramanathan V (2017) Well below 2oC: Mitigation strategies for avoiding dangerous to catastrophic climate changes, Proc Natl Acad Sci U.S.A 114: 201618481.
88. Duscha V, Denishchenkova A, Wachsmuth J (2018) Achievability of the Paris Agreement targets in the EU: demand-side reduction potentials in a carbon budget perspective, Clim Pol 3062: 1-14.
89. Fuglestvedt J, Rogelj J, Millar RJ, Allen M, Boucher O, et al. (2018) Implications of possible interpretations of greenhouse gas balance in the Paris Agreement, Philos Trans R Soc A 376: 20160445.
90. Zhou S, Liu Y, Li J, Wang Y, Jiang et al. (2014) Facile in situ synthesis of graphitic carbon nitride (g-C3N4)–N-TiO_2 heterojunction as an efficient photocatalyst for the selective photoreduction of CO_2 to CO, Appl Catal B 158-159, 20-29.
91. Jia J, O'Brien PG, He L, Qiao Q, Fei T, et al. (2016) Visible and Near-Infrared Photothermal Catalyzed Hydrogenation of Gaseous CO_2 over Nanostructured Pd@Nb_2O_5, Adv Sci 3: 1600189.
92. Meng X, Wang T, Liu L, Ouyang S, Li P, et al. (2014) Photothermal Conversion of CO2 into CH4 with H-2 over Group VIII Nanocatalysts: An Alternative Approach for Solar Fuel Production, Angew Chem Int Ed 53: 11478-11482.
93. Mateo D, Albero J, Garc´ıa H (2018) Graphene supported NiO/Ni nanoparticles as efficient photocatalyst for gas phase CO_2 reduction with hydrogen, Appl Catal B 224: 563-571.